Nanostructures in austenitic steel after EDM and pulsed electron beam irradiation

J.W. Murray [a], J.C. Walker [b], A.T. Clare [a,*]

[a] Institute for Advanced Manufacturing, Department of M3, University of Nottingham, Nottingham NG7 2RD, UK
[b] National Centre for Advanced Tribology Southampton (nCATS), University of Southampton, Southampton SO17 1BJ, UK

ABSTRACT

The resulting recast layer from EDM often exhibits high levels of residual stress, unacceptable crack density and high surface roughness; all of which will contribute to diminished surface integrity and reduced fatigue life. Previous studies have shown that the surface of EDM'd components can be successfully enhanced through the use of large-area pulsed electron beam surface modification, which, through a rapid remelting process, results in a net smoothing of the workpiece surface. It has also been shown that cracks created by EDM are repaired within the region molten by EB irradiation, and therefore the process is proposed to reduce the impact of EDM on fatigue life and deleterious surface properties. In this work the complex multilayers of the near surface are interrogated by TEM and XRD. A FIB-TEM study of the entire remelted layer produced by the irradiation process has been performed for the first time. The characterisation of these layers is necessary for predicting the performance of the material in application. Pulsed EB irradiation was shown to be capable of creating several distinct surface layers of nanostructures which consist of varying grain sizes and grain orientations. Austenite was revealed as the dominant phase in the remelted layer, with a grain size as small as 5 nm produced at the very top surface. A needle-like phase also present in the layer is thought to be cementite.

© 2014 The Authors. Published by Elsevier B.V. This is an open access article under the CC BY license (http://creativecommons.org/licenses/by/3.0/).

1. Introduction

Unlike conventional machining processes which rely upon shear based mechanisms for material removal, electrical discharge machining (EDM) liberates material from the bulk workpiece through rapidly heating and melting localised regions. Once removed the surface of the workpiece is characterised by a pattern of craters and often a wavy surface characteristic of metal flow on the surface. The process is useful for the machining of high-value components such as mould tools and dies as well as aerospace engine components. The process is particularly advantageous when compared to conventional mechanical cutting operations since strength and toughness of the workpiece are not factors in its machinability, and instead the thermal and electrical properties determine the ability for a material to be cut. In EDM complex features can be produced using a single tool electrode of mirrored geometry, or a continuously spooling wire electrode in the case of wire-EDM.

EDM is known to significantly affect the surface of cut materials compared to many other manufacturing processes such as milling,

grinding or electrochemical machining, and the reduced potential fatigue life of EDM'd components has led to the common perspective that the surface should be at least partially removed [1]. The EDM process involves the repeated expulsion of molten and vaporised material at the end of every discharge, typically several thousand times per second, causing some material to resolidify on the workpiece surface and leaving a recast layer to remain. This region is characterised by cracks and a rough surface morphology consisting of pits and asperities limiting corrosion resistance, and these defects combined with high tensile residual stresses impede mechanical behaviour such as fatigue and tribological performance. Several authors have noted the negative effect of EDM on the fatigue life of machined alloys. Zeid [2] observed that roughing EDM conditions corresponding to higher currents and pulse-on times can result in a reduction in the number of life cycles to failure in tool steel by up to 50%. It was determined that the presence of surface cracks caused by EDM effectively eliminated the crack initiation phase of the failure process thereby reducing fatigue life. Tai and Lu [3] further investigated the relationship between EDM surface characteristics and fatigue life and identified that parameters which increased the prevalence of surface cracks were a reduced current and increased discharge time, and the surface which contained cracks exhibited the worst fatigue life.

The pulsed electron beam irradiation process for surface melting is an effective method of rapidly improving the surface finish and

* Corresponding author at: Room A49 Coates, University Park, Nottingham NG7 2RD, UK. Tel.: +44 115 951 4109.
E-mail addresses: epxjm2@nottingham.ac.uk (J.W. Murray), j.walker@soton.ac.uk (J.C. Walker), kjames.murray@nottingham.ac.uk (A.T. Clare).

morphology of an EDM'd steel surface [4]. It has been shown that under the correct choice of parameters (a cathode voltage of 35 kV and 20 irradiation shots), the EDM induced recast layer can be treated such that cracks are eliminated by incremental repair due to surface tension effects, as well as creating an improved surface finish. Some preliminary observations were also made regarding phase changes in the remelted surface using XRD analysis; however no detailed metallurgical study has been performed yet to investigate phase changes, grain size, grain orientation and their relation to depth from the surface.

Since rapid cooling rates are observed after surface melting by the irradiation process (10^8–10^9 K/s), novel microstructural changes such as nanostructures are also expected. Since the remelted surface layer in a steel sample with repaired cracks has a thickness of approximately 4.0 μm, transmission electron microscopy (TEM) is necessary for detailed microstructural characterisation.

Previous microstructural characterisation and particularly TEM interrogation of the remelted surface caused by pulsed EB irradiation are limited, although many authors have observed preferential grain orientation at the surfaces of alloys treated by pulsed electron beam irradiation using XRD analysis. Okada et al. [5] used TEM to image the grain structure of the remelted layer in SUS420J2 steel subjected to EB irradiation, and it was observed that significant grain size reduction occurred. Despite this the scope of the imaging was limited, and the location of the image taken was not presented in relation to the top surface of the sample, nor was the identity of the grains shown. Proskurovsky et al. [6] and Pogrebnjak [7] have examined TEM images of a ferritic steel and single crystal copper respectively, revealing nanostructures down to 30 nm induced by the irradiation process for example in steel, however there is still no clear cross-sectional TEM analysis of the entire remelted layer from the top surface revealing the evolution of microstructures with depth. Such a study is necessary to clearly summarise the range of structures expected after EB irradiation. It is also thought that an investigation of the scale of structures and their relation to depth will help elucidate the scale and direction of cooling gradients beneath the irradiated surface. For the application of pulsed electron irradiation to surface finishing of EDM'd components exhibiting a 'damaged' recast surface layer, the potential mechanical properties of the surface layer such as fatigue, fretting fatigue and wear behaviour can only properly be explained by its metallurgical properties.

In Fig. 1 the improvements in surface morphology, crack proliferation and the mechanism of this crack repair process can be observed.

This study therefore continues this work, and the EDM parameters which resulted in a cracked surface were used again in this study, to demonstrate the usefulness of the irradiation process on a damaged machined surface. Therefore in this study, the optimum electron irradiation parameters which result in the crack repair process on such surfaces will be examined here using TEM and XRD.

2. Experimental

2.1. EDM process and material

A Sodick AP1L micro die-sink EDM machine was used to machine the initial 6 × 6 mm shallow slot and induce a typical recast surface on the sample. The same machining settings used in previous work by the authors were used [4], including a kerosene dielectric and positive electrode polarity to best represent a typical micro-EDM setup. In this previous study, EDM parameters were investigated and chosen in order to induce a recast layer with a high number of surface cracks. In order to emulate these conditions under which material removal rate was high but a significant surface crack density was produced, the EDM settings shown in Table 1 were used.

The workpiece material used was AISI 310 stainless steel, an austenitic general purpose steel. Its etched microstructure can be seen in Fig. 1(a). The initial composition before electrical discharge machining can be seen in Table 2.

2.2. Pulsed electron beam irradiation process

In previous work, the irradiation parameter of 20 shots at 35 kV was identified to produce the uniform, crack-free surface seen in Fig. 1(c). Therefore for this study, the same parameter settings were used to modify the EDM'd surface for XRD and TEM interrogation. This set of parameters can be seen in Table 3.

A Sodick PF32A EBM machine was used for electron beam irradiation experiments (schematic in Fig. 2). The irradiation process is carried out in an air-tight chamber into which an inert gas, argon at a pressure of 0.05 Pa is supplied, after an initial 10 minute vacuum cycle time. This argon gas is used as the medium for plasma buildup required for the electron generation and beam propagation. Bombardment of the high current electrons with a workpiece causes rapid heating and cooling cycles at its surface. The diameter of the beam is 60 mm; with a pulse-time
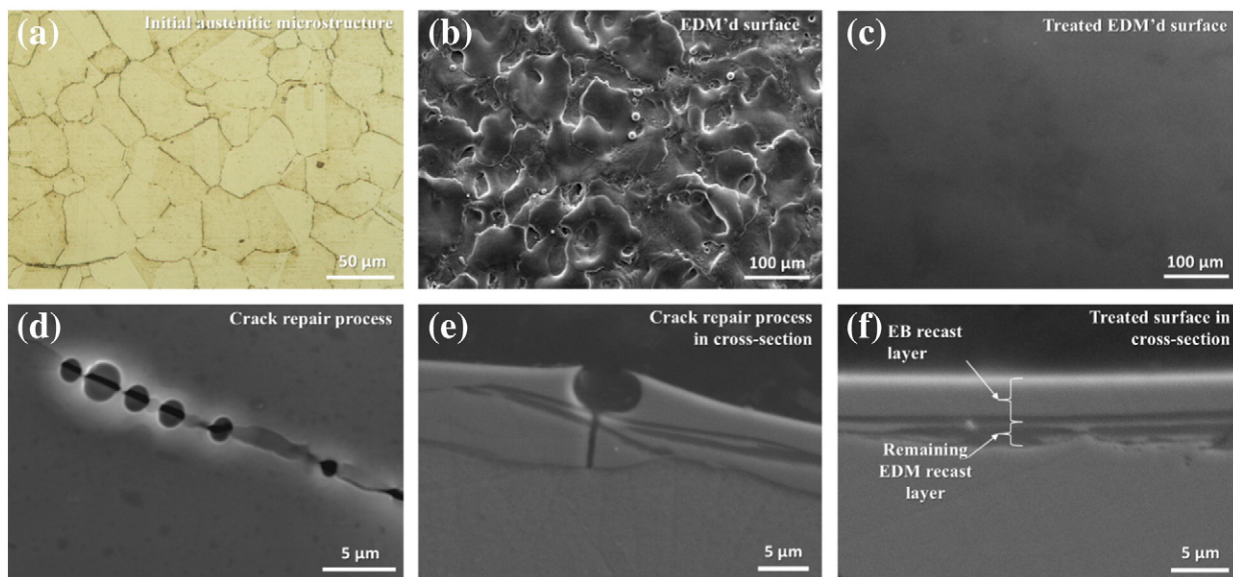

Fig. 1. (a) Initial microstructure of the austenitic workpiece, (b) and (c) morphologies of a typical EDM'd surface before and after irradiation, (d) and (e) crack repair process observed to cause the elimination of cracks in irradiated surface and (f) fully treated surface in cross-section [4].

Table 1
EDM parameters.

Electrode polarity	On-time (μs)	Off-time (μs)	Main current (A)	Gap voltage (V)	Capacitance
+	30	3	4.5	90	Stray

of 0.8–3 μs [8] and pulse interval of 11 s. The beam has been shown to extend further than its 60 mm diameter although the energy density is significantly diminished beyond this point. Within the 60 mm diameter, energy density has shown to be uniform [9].

A more detailed description of the workings of the machine can be found in work from the inventors of this technique, for example in [8]. Firstly a solenoid coil produces a magnetic field, at the maximum intensity of which a pulsed voltage of 5 kV is applied to the anode and Penning discharge is initiated. After a duration of 50–100 μs, the current of the Penning discharge reaches 150–170 A, and a plasma column is formed near the anode. After a delay time of 10–30 μs, an accelerating voltage of up to 40 kV (on the Sodick AP1L) with a rise time of 20–100 ns is applied to the cathode. The electric field is concentrated in a near-cathode ion layer and reaches values of up to 400 kV/cm. Explosive emission takes place on the cathode causing a number of cathode spots (dense plasma clouds) to appear and emit electrons. The applied voltage is concentrated in a double-layer, between the cathode plasma and the anode plasma, in which the electrons are accelerated and the beam is formed. The electron beam accelerated in the double layer is transported through the anode plasma to a collector cathode where the workpiece is placed.

2.3. XRD and TEM

X-ray diffraction was performed using a Bruker AXS "D8 Advance" diffractometer, producing Cu k-alpha monochromatic radiation. For standard XRD, the diffractometer was rotated from 40° to 100° with a step value of 0.04° and a step time of 2 s. For the glancing angle, the same 2 theta values were used, but with a step value of 0.02° and a dwell time of 8 s at each step.

Focused ion beam (FIB) milling using an FEI Quanta 200 3D FIBSEM was performed to prepare two lamellae from the irradiated surface. Preparation of one lamellar with a sufficient depth into the sample as well as with sufficient thinness proved difficult as thinning of a large area of the lamellar inevitably resulted in damage to the topmost edge of the lamellar. For this reason, two lamellae were prepared, one with approximately 100 nm in thickness, representative of the first 3 μm into the sample, and the second slightly thicker and representing depth into the sample between 1 and 6.5 μm. TEM was performed with a JEOL 2100F at 200 kV using both bright field (BF) and dark field (DF) imaging.

3. Results

3.1. Grain size and orientation

The near-surface lamellar was first analysed using TEM in order to determine the grain size, grain orientation as well as depths of sub-layers associated with the transformations induced by the pulsed electron beam irradiation process.

Fig. 3 shows bright-field and dark-field TEM cross-sectional images of the irradiated sample from the surface to a depth of 3 μm. Selected-area diffraction patterns (SAED) accompany the images to reveal a fine polycrystalline structure. A clear ringed pattern indicates a polycrystalline structure with no preferential orientation. In the dark-field image, this structure can be observed particularly clearly as the image is composed of a fine mixture of dark contrast and light contrast regions, suggesting a random distribution of grains. This polycrystalline structure is maintained between the top surface and approximately 1 μm depth. In the TEM images, between 1 and 2 μm depths, grains are noticeably coarser. A randomised grain structure is also still indicated by SAED patterns, however the polycrystalline rings are composed of fewer individual spots, meaning fewer grains are contributing to the whole pattern over the same total area contributing to the pattern, suggesting a larger grain size.

To quantify grain sizes within the two randomly oriented polycrystalline regions; between 0 and 1 μm, and between 1 and 2 μm depths, the diameters of 100 individual grains were measured in each region and were plotted in histogram format, as shown in Fig. 4.

Within the first 1 μm depth, the modal (most frequent) grain size was between 15 and 20 nm. This can be compared with the region between 1 and 2 μm depths, in which the modal grain size was between 25 and 30 nm. Interestingly, the finest grain sizes of between 5 and 10 nm were seen in both regions, although this size range was three times more frequent in the top region of the lamella. The largest grain size observed in the top region was 43 nm, whereas a single 145 nm grain was seen in the deeper region. The median grain size between 0 and 1 μm depths was 18 nm, and the mean value was 19 nm. Between 1 and 2 μm depths, the median value was 42 nm, with a mean of 46 nm. Despite larger grain sizes only being observed in the region between 1 and 2 μm depths, the finest grain sizes of between 5 and 10 nm were seen in both the near surface region and as far as the 2 μm depth.

Beyond the 2 μm depth, a single-orientation region was observed. This can be seen as the uniform, dark contrast region, beneath the polycrystalline region in the dark field image in Fig. 3. In Fig. 5, a higher magnification image of this single-orientation region can be seen. Columnar grains between 50 and 100 nm width can be observed in a direction perpendicular to the surface, from a depth of approximately 2 μm to 3 μm. A selected area diffraction pattern with a diameter of 1 μm, incorporating several grains yields a single phase pattern with a single orientation.

For TEM analysis of the region beneath 3 μm the second lamellar was interrogated. A bright-field image of the entire depth of this lamellar can be seen in Fig. 6. In this sample, a polycrystalline region also followed by a section of columnar grains can be seen at the top of the image. In this lamellar however a number of needle structures were observed which cross the boundary between the polycrystalline region and the columnar region beneath.

Beneath the sub-layer of columnar grains is a polycrystalline region with random orientation, this is evidenced by both the varying dark and light contrasts of grains in this layer, and the dominant polycrystalline rings of the associated SAED pattern. A large variation in grain size is present in this region, with grains in the size range of 40–250 nm in diameter. Beneath this is the interface between the remelted layer due to electron irradiation, and the layer beneath is assumed to be caused by the EDM process and not as a result of EB irradiation. The interface is present at a depth of 4.0 μm from the top surface, and this was consistent with that measured in previous work with the same irradiation parameters, by SEM imaging [4]. Beyond this interface, from a depth of 4.0 μm to the end of the lamellar at 6.0 μm depth, a more consistent

Table 2
AISI 310 stainless steel composition before EDM and EB irradiation (wt.%).

Fe	Cr	Ni	Mn	Si	Co	Cu	C	N	P	Nb	S
Balance	25.61	19.21	0.92	0.59	0.12	0.11	0.046	0.04	0.016	0.003	0.001

Table 3
EB parameters.

Cathode voltage (kV)	Energy density (J/cm^2)	Number of shots	Anode voltage (kV)	Solenoid voltage (kV)	Argon pressure (Pa)	Irradiation distance (mm)
35	13.5	20	5	1.5	0.05	300

grain structure, consisting of grains between 200 and 400 nm in diameter remains. A SAED pattern incorporating multiple grains in this region yields a purely single phase pattern indicating a single preferential orientation. The uniform contrast of these grains in bright-field mode also highlights their oriented structure.

3.2. Phase identification

Fig. 7 shows indexed SAED patterns from both the very top surface in the region of the finest grain size, and from the region of columnar grains as seen in Fig. 5. For convenience, the schematic in Fig. 9 should be referred to for ease of locating the SAED patterns shown in Fig. 7.

A number of SAED patterns were taken from the fine polycrystalline region on the first (top) lamellar; all were indexed as consistent with FCC austenite. The pattern in Fig. 7(b) is from the columnar grain region at the bottom of the top lamellar, beneath the randomly oriented polycrystalline region. This crystalline pattern was also identified as belonging to FCC austenite. The polycrystalline pattern in location 1 in Fig. 6 was also identified as austenite, sharing the same pattern as seen in Fig. 7(a). Despite this, the pattern was expectedly composed of fewer dots, given the larger grain size and therefore fewer orientations contributing to the pattern.

From the second, deeper lamellar imaged in Fig. 6, identification of the needle structures at the top of the image was difficult given their small area available for yielding diffraction patterns, resulting in surrounding structures forming the majority of any patterns, and the fact that little diffraction was being caused by these structures, as evidenced by their bright contrast in bright field imaging. Several grains were used to produce a SAED pattern corresponding to location 2 in Fig. 6. The resultant pattern, seen in Fig. 7(c), despite consisting of multiple grains, is of a single orientation, and also corresponds to FCC austenite. This region of austenite continues until the bottom of the lamellar, 6.0 μm from the top surface.

3.3. XRD

Although TEM is the best method of deeply characterising small regions of a material, the technique is inherently localised and not necessarily representative of the entire region of the 6 × 6 mm machined sample. XRD and glancing-angle XRD are useful non-destructive methods of confirming the dominant phases and phase changes occurring at the surface of the sample, and in particular the needle structures not confirmed with SAED patterns may be identified using GAXRD. Fig. 8 shows the X-ray spectra using both standard XRD and GAXRD. XRD was performed on a polished sample of the as-received steel, an EDM'd surface and a treated EDM'd surface, i.e. the same sample used for the TEM analysis. GAXRD was performed on the EDM'd surface and the treated surface.

Standard XRD alone typically penetrates to a depth which highlights the phases which dominate the EB remelted layer, however, the shallower depths penetrated using GAXRD can further reveal whether these phases are present in the same ratios within the uppermost 400 nm. Table 4 lists the penetration depths from which 90% of the X-ray signal arises based on the composition of the initial 310 steel (although it should be noted that the carbon value is expected to increase after EDM). Fig. 8 shows both standard XRD and GAXRD patterns, and possible phases and planes are labelled.

Since the depth of the EB remelted layer in the sample used in this study is approximately 4.5 μm, it is clear that the standard XRD signal is almost entirely inside this layer, based on the penetration depths in Table 4. Based on standard XRD, FCC austenite is the dominant phase after both EDM as well as after EDM then electron irradiation. After irradiation the austenite peaks become more dominant. Under GAXRD, the peak to the right of the (111) austenite peak is larger relative to the austenite peaks, compared to under standard XRD, indicating that the corresponding phase is more prevalent with the first few hundred nm from the surface. The location of this peak may correspond to orthorhombic cementite, indicating that the needle structures are of this phase, although there is a BCC peak at close proximity. Under EDM only, this proposed cementite peak is stronger and sharper. It can however be concluded that FCC austenite is the dominant phase both in the first 4.69 μm and in the first 400 nm, and the ratio between the FCC peaks is lessened after irradiation, supporting the randomisation of grain orientations.

4. Discussion

Given the complex nature of the sub-layers observed in TEM imaging of the irradiated surface, a schematic detailing the structures identified can be seen in Fig. 9. Phases, approximate depth into the sample, grain size and orientation are summarised here.
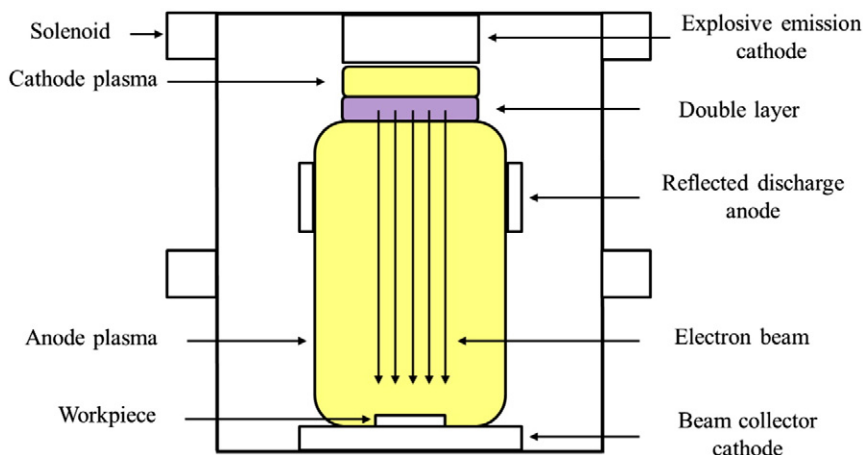

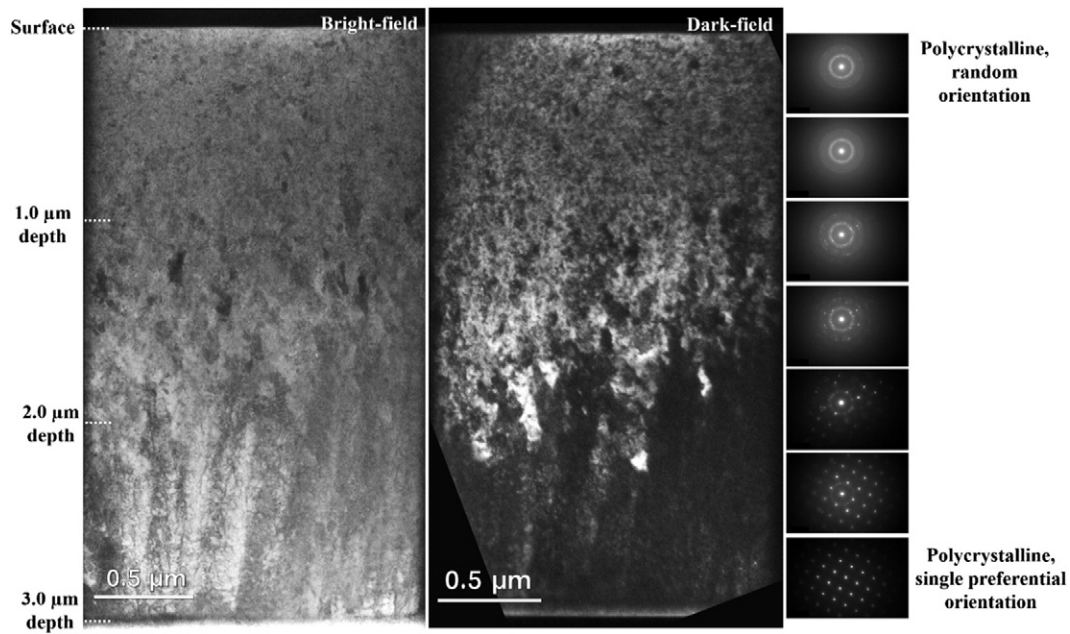**Fig. 2.** Schematic of 'EBM' irradiation process.

Fig. 3. Bright-field and dark-field TEM images of a cross-section from the surface to 3 μm depth. SAED patterns expose random orientation close to the surface, and a single orientation beneath this. The interface between these regions is clearly exposed in DF mode.

The near-surface structure of the EDM'd sample subject to 20 irradiation shots at 35 kV is characterised by nanograined austenite. Stähli and Sturzenegger [10] showed the production of thin boundary layers of homogenous austenite after laser-pulse irradiation. The presence of very fine retained austenite in steel after pulsed electron irradiation has also been reported elsewhere [11,12]. It is thought that the cooling rate avoids the martensitic phase transformation, as well as preventing further growth in size of the austenite grains. It is also expected that an increased carbon content, as is the case after EDM in oil, suppresses the formation of martensite. Since it was observed that after 1 μm depth from the surface, austenite grains are clearly larger, it is thought that the cooling rate in this location is reduced compared to immediately next to the surface. It has been shown by calculation that after pulsed electron beam irradiation the temperature is always the highest at the very top surface [13]. Okada et al. [14] proposed that under an energy density of 12.0 J/cm^2, the theoretical temperature at the top surface of SKD11 tool steel can reach approximately 13,000 K, and 4 μm beneath

the top surface the temperature reaches a maximum of approximately 7000 K, above the boiling point of virtually any metal. The highest rate of quenching from the melt and the highest velocity of the crystallisation front are expected at the surface (10^9 K/s and 5 m/s respectively) [15] and therefore such a grading of nanostructures is also expected.

Fine plate structures (a needle-like shape in cross-section) within the top 2.5 μm were also observed. These structures appear to have grown from the interface between the randomly oriented austenite and the columnar austenite beneath this, at approximately 2.5 μm depth from the surface. GAXRD patterns suggest that these may be cementite needles in a nanocrystalline austenite matrix. It should be noted that such needle structures were only observed in one of the
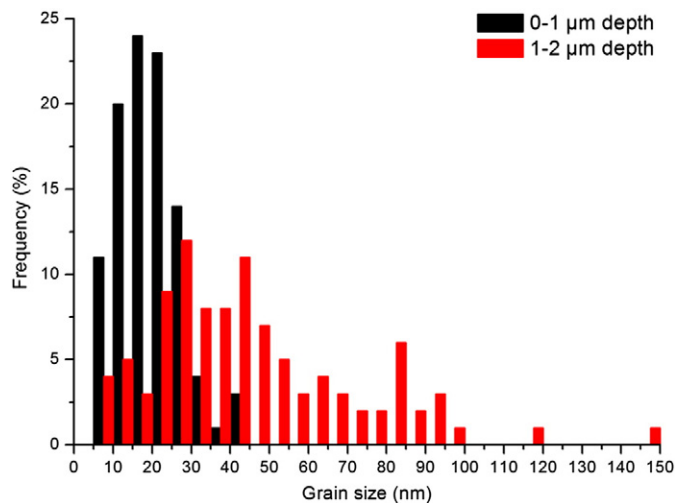

Fig. 4. Histogram plots of grain sizes between the surface and 1 μm depth, and between 1 and 2 μm depths.
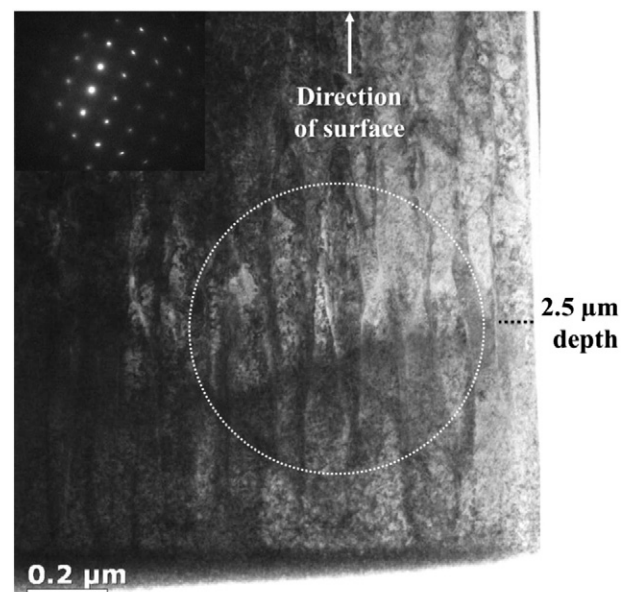

Fig. 5. Bright-field image and associated SAED pattern of columnar grains with single preferential orientation between 2 and 3 μm beneath the top surface.
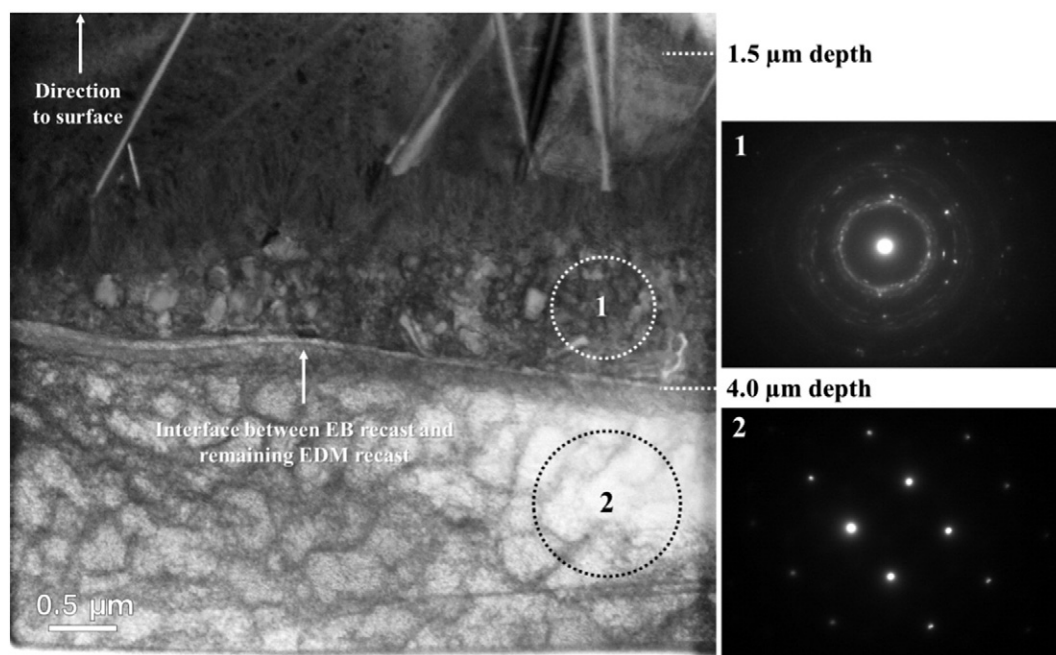
Fig. 6. Bright-field image showing complex sub-layers, including the EB/EDM interface.

two lamellae. This may be related to the inhomogeneity of the level of carbon absorption during the EDM process from the oil based dielectric, effectively resulting in a slightly different composition in the locations of the two lamellae. It is also known that both tool and carbon contamination in the recast layer during EDM are not completely uniform at the nanometre scale [16]. Absorption of carbon into the EDM recast layer during machining increases the stability of the cementite phase. The absence of martensite in the remelted layer would also be consistent with the results of Proskurovsky et al. [15] using a carbon steel (Steel 45) treated by EB irradiation.

An entirely austenitic region was also observed beneath what is thought to be the EDM–EB interface. It is assumed that the microstructure here is unchanged from before EDM, given that they appear to be beneath the melt zone induced by irradiation. An austenitic microstructure of the EDM'd surface of steel is expected when machining in an oil dielectric, as was the case in this study, for example by Kruth et al. [17], who also observed that significant cementite dendritic structures were formed, inferring that the uptake of carbon from the dielectric is significant enough to cause the formation of iron carbides, given that it was

found that carbon content in the surface increased four-fold during machining in oil. There has also been evidence of cementite seen in the TEM/XRD study of carbon steel subject to EDM by Cusanelli et al. [18]. This may support the identification of a strong cementite XRD peak for the EDM'd only surface.

If we consider the XRD diagrams in Fig. 8, and the apparent cementite peak in Fig. 8(b), the peak is much sharper and relatively large compared to after EB irradiation. The initial formation of cementite after EDM is expected based on the uptake of carbon during machining. The relatively large size of the cementite peak before irradiation fits with the formation of cementite by EDM. Guan et al. [11] determined that for pulsed electron irradiation of a carbon steel at 4 J/cm^2, and assuming a melt lifetime of 10^{-5} s, a carbon diffusion distance of 0.3 μm can be estimated. If we consider that the diffusion distance in this work is on the same order of magnitude as this value, the distance is still larger than the grain size of the resultant austenite grains after irradiation. It is likely that the formation of nanograined austenite which dominates the remelted layer was encouraged by the dissolution of any carbide formed after the EDM process, with the presence of carbon
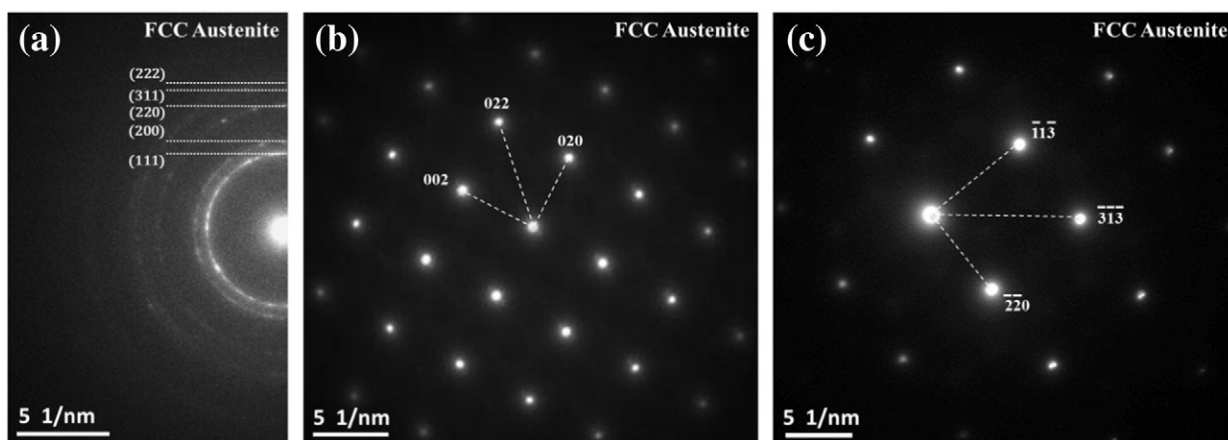

Fig. 7. Refer to Fig. 9 for the location of patterns — (a) FCC polycrystalline SAED pattern taken 100 nm from the top surface, (b) FCC SAED single orientation pattern taken from multiple grains approximately 2.5 μm from the top surface and (c) FCC pattern taken from below the EB–EDM interface.
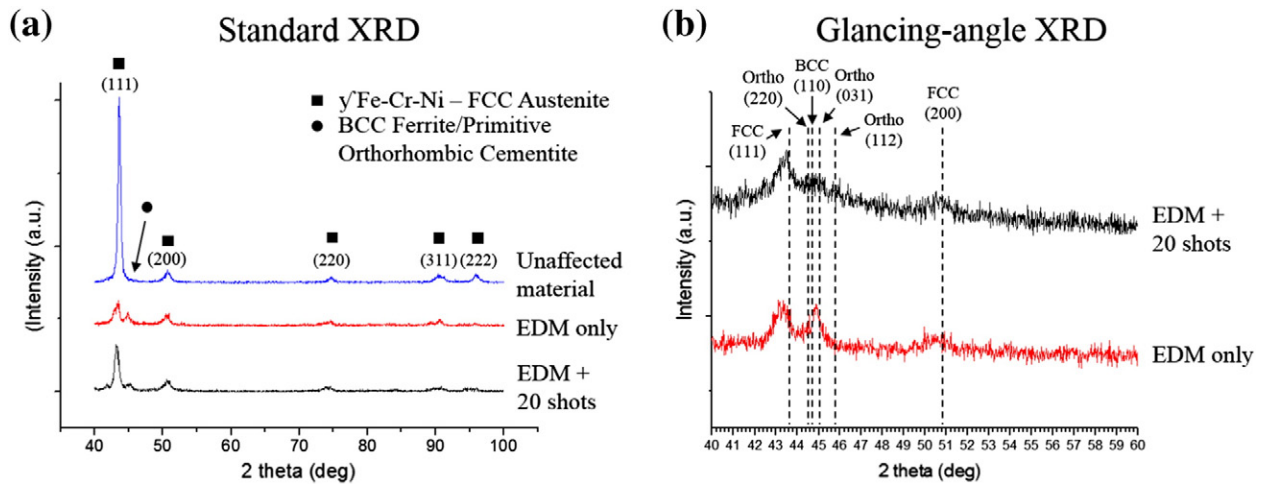
Fig. 8. (a) XRD patterns of the unaffected material, the EDM'd surface and the EDM'd surface irradiated with 20 shots at 35 kV and (b) glancing angle XRD patterns of the EDM'd surface and the irradiated EDM'd surface.

increasing the stability of the austenite phase. The dissolution of carbides and diffusion of carbon during heating by EB irradiation would explain the absence of cementite in one of the two lamellas, and the inhomogeneity of the cementite structures. Proskurovsky et al. also note that in austenitic 304 stainless steel treated by pulsed EB irradiation, the original particles of secondary phases such as carbides and intermetallic compounds dissolve in this layer either partially or completely, supporting the scarcity of secondary phases in the layer observed in this work [15].

It has been shown that a nanostructured layer at the surface of carbon steel can improve its surface hardness and fatigue strength [19]. Similarly, a nanocrystallised surface on 316L stainless steel was shown to increase its surface hardness by almost three times [20]. In the former study, surface mechanical attrition treatment was used, utilising the vibration of steel balls, typically 1–10 mm in diameter [21], larger than those used in shot peening, to induce significant plastic deformation and effective grain sub-division. The latter study used fast multiple rolling rotation, a plastic deformation process using static pressure to introduce a nanocrystalline surface on a large sample. Both of these processes are limited from application on components with a small surface or with delicate surface structures, whereas pulsed electron beam irradiation is a more suitable process for the surface treatment, modification and introduction of fine nanostructures on highly intricate surfaces.

5. Conclusions

- A cross-sectional FIB-TEM study of the entire remelted layer formed by pulsed electron beam irradiation has been performed for the first time.
- A graded nanostructure has been shown to be formed in the first 4 μm of the surface of austenitic stainless steel subject to pulsed electron beam irradiation after electrical discharge machining, with a grain size down to 5 nm at the very top surface.
- A random orientation of austenite grains is seen within the first 2 μm, with a needle-like phase thought to be cementite present within this

Table 4
XRD penetration depths for 90% of signal in μm, at different 2 theta values.

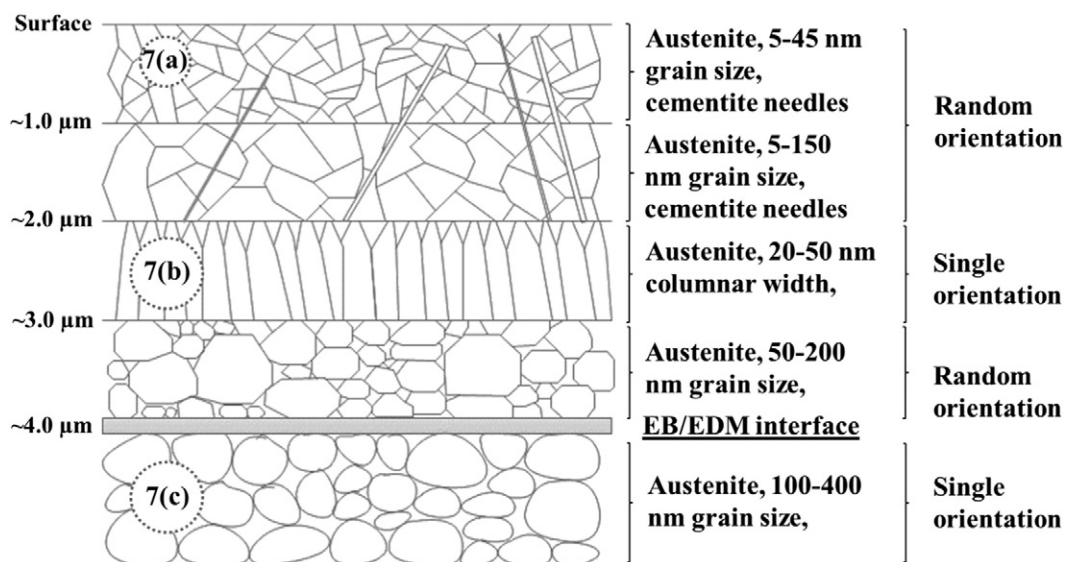|	100°	60°	40°	30°
Standard XRD	4.69	3.06	2.09	1.58
Glancing angle	0.41	0.41	0.40	0.40

Fig. 9. Schematic of sub-layers of electron beam irradiated EDM'd steel. Indexed patterns of labelled areas can be seen in Fig. 7.

matrix, below which is a single orientation region of columnar austenite grains, followed by a region of randomly oriented austenite grains beneath this.

- Carbon absorption after EDM, and its subsequent diffusion during EB irradiation is thought to contribute to the stability of the dominant nanograined austenite phase formed by the rapid heating and cooling cycle associated with the treatment process.
- A sharp interface can be seen between the EB remelted layer and the remaining EDM recast layer beneath, which is composed of solely single-orientation polycrystalline austenite until at least 6.0 μm depth.

Acknowledgements

References

[1] F. Klocke, D. Welling, J. Dieckmann, Procedia Eng. 19 (2011) 184–189.
[2] O.A.A. Zeid, J. Mater. Process. Technol. 68 (1997) 27–32.
[3] T.Y. Tai, S.J. Lu, Int. J. Fatigue 31 (2009) 433–438.
[4] J.W. Murray, A.T. Clare, J. Mater. Process. Technol. 212 (2012) 2642–2651.
[5] A. Okada, Y. Uno, J.A. McGeough, K. Fujiwara, K. Doi, K. Uemura, S. Sano, CIRP Ann. Manuf. Technol. 57 (2008) 223–226.
[6] D.I. Proskurovsky, V.P. Rotshtein, G.E. Ozur, Surf. Coat. Technol. 96 (1997) 117–122.
[7] A.D. Pogrebnjak, S.M. Duvanov, A.D. Mikhaliov, V.I. Lavrentiev, V.V. Stayko, A.V. Markov, Y.F. Ivanov, V.P. Rotstein, D.I. Proskurovsky, Surf. Coat. Technol. 89 (1997) 90–96.
[8] A.V. Batrakov, A.B. Markov, G.E. Ozur, D.I. Proskurovsky, V.P. Rotshtein, Eur. Phys. J. Appl. Phys. 43 (2008) 283–288.
[9] Y. Uno, A. Okada, K. Uemura, P. Raharjo, T. Furukawa, K. Karato, Precis. Eng. 29 (2005) 449–455.
[10] G. Stähli, C. Sturzenegger, Scr. Metall. 12 (1978) 617–622.
[11] Q.F. Guan, H. Zou, G.T. Zou, A.M. Wu, S.Z. Hao, J.X. Zou, Y. Qin, C. Dong, Q.Y. Zhang, Surf. Coat. Technol. 196 (2005) 145–149.
[12] Y. Ivanov, W. Matz, V. Rotshtein, R. Günzel, N. Shevchenko, Surf. Coat. Technol. 150 (2002) 188–198.
[13] Y. Qin, J. Zou, C. Dong, X. Wang, A. Wu, Y. Liu, S. Hao, Q. Guan, Nucl. Instrum. Meth. B 225 (2004) 544–554.
[14] A. Okada, Y. Okamoto, Y. Uno, K. Uemura, J. Mater. Process. Technol. 214 (2014) 1740–1748.
[15] D.I. Proskurovsky, V.P. Rotshtein, G.E. Ozur, Y.F. Ivanov, A.B. Markov, Surf. Coat. Technol. 125 (2000) 49–56.
[16] J.W. Murray, M.W. Fay, M. Kunieda, A.T. Clare, J. Mater. Process. Technol. 213 (2013) 801–809.
[17] J.P. Kruth, L. Stevens, L. Froyen, B. Lauwers, CIRP Ann. Manuf. Technol. 44 (1995) 169–172.
[18] G. Cusanelli, A. Hessler-Wyser, F. Bobard, R. Demellayer, R. Perez, R. Flükiger, J. Mater. Process. Technol. 149 (2004) 289–295.
[19] D. Li, H.N. Chen, H. Xu, Appl. Surf. Sci. 255 (2009) 3811–3816.
[20] P. Chui, K. Sun, C. Sun, X. Yang, T. Shan, Appl. Surf. Sci. 257 (2011) 6787–6791.
[21] K. Lu, J. Lu, Mater. Sci. Eng. A 375–377 (2004) 38–45.